Nanocrystalline anatase derived from modified alkoxide mesostructured gel

S. Kurajica[1] · I. Minga[1] · V. Mandić[1] · G. Matijašić[1]

Abstract A sol prepared by chelation of titanium *n*-butoxide with ethyl acetoacetate (1:1) was slowly hydrolyzed, and the obtained gel was thermally treated in order to produce anatase. Samples were investigated by means of FTIR, XRD, DTA/TG, N_2 adsorption–desorption isotherms, FESEM and HRTEM. It was determined the modified alkoxide is partially hydrolyzed, leaving small amount of butoxide and ethyl acetoacetate groups attached to titanium. XRD pattern and HRTEM micrograph revealed gel ordering at the mesostructure scale. Observed mesostructure was found to be consisted with inorganic–organic nanoclusters, exhibiting some polydispersity in the size and variations in composition. Thermal decomposition exhibits evaporation of water and butanol, elimination of ethyl acetoacetate and butoxy groups, carbonate removal, anatase crystallization and transformation to rutile, accompanied with oxidation of carbonaceous species. After 2 h at 350 °C pure nanocrystalline anatase crystallites were obtained having average crystallite size of 16.4 nm with majority of exposed {101} facets.

Keywords Anatase · Chelating agent · Hybrid nanoclusters · Mesoporous gel · Nanocrystals

Introduction

Nanocrystalline titania powders were widely studied with respect to potential photocatalytic, photovoltaic and optical applications [1]. It is well accepted that the performance of titania depends on many parameters such as phase composition, crystallinity, morphology and texture [2–4]. Among three polymorphs associated with titanium dioxide, anatase is widely regarded to be the most effective photocatalyst [3, 5]. Hence, the synthesis of pure anatase nanoparticles is of great technological interest.

Nanocrystalline titania is often synthesized through sol–gel process using titanium alkoxide precursors. Sol–gel process involves first hydrolysis and condensation of the metal alkoxides to be followed by treatment at elevated temperature in order to produce ceramics. Processing at low temperatures, purity and tailoring of the material properties are among most important advantages offered by the sol–gel technology.

Due to the strong reactivity of the alkoxides with water, this process would result in an uncontrolled precipitation [6]. The chemical modification with chelating agents yields the precursors stability increase and thus enables better control of hydrolysis and condensation steps [7]. The structure of modified alkoxide further affects the properties of gel formed by its hydrolysis, which is reflected in physical properties of the final material.

Various chelating agents can be used for the chemical modification of metal alkoxides, and among them β-diketones and β-ketoesters, due to availability and low cost, are the most commonly used [8–10]. β-Diketones and β-ketoesters are bidentate monocharged ligands capable of undergoing the keto–enol tautomerism. Most often the ketonic form predominates, while in the presence of alkoxide, the reactive enol form of Eaa substitutes the alkoxy

✉ S. Kurajica
stankok@fkit.hr

[1] Faculty of Chemical Engineering and Technology, University of Zagreb, Marulicev trg 19, 10000 Zagreb, Croatia

groups of alkoxide, forming six-membered chelate ring strongly shifting keto–enolic equilibrium toward the enolic form [11].

In our previous study [12], we prepared four gels using titanium n-butoxide, Tnb (Ti(O^{n}Bu)$_4$), and ethyl acetoacetate, Eaa (C$_6$H$_{10}$O$_3$), with Eaa/Tnb molar ratios of 0.5, 1, 1.5 and 2. Gels showed similar X-ray diffraction patterns, FTIR spectra and crystallization behavior [12]. Therefore, in the present study, a sample with Eaa/Tnb molar ratio of 1 has been taken as representative and investigated in order to obtain closer insight in the gel microstructure, thermal degradation process, as well as properties of titania crystallized thereof.

Materials and methods

The sol was prepared using titanium n-butoxide, Tnb (Ti(O^{n}Bu)$_4$), (98 %, Alfa Aesar, Germany), ethyl acetoacetate, Eaa (C$_6$H$_{10}$O$_3$, 98 %, Fluka, Germany), while isopropyl alcohol (C$_3$H$_7$OH, 99 %, Kemika, Croatia) was used as a solvent. The appropriate amount of Eaa (0.1 mol) was firstly added to the 0.5 mol of solvent, and then, 0.1 mol of Tnb was dissolved in solvent/Eaa solution. Tnb was added to the solution using syringe to minimize exposure to air humidity. The mixture was stirred in a closed reactor for 24 h at room temperature, and no precipitation was observed. The clear sol was poured into a large Petri dish in order to maximize exposure to air moisture and kept at room temperature until gelation. Drying of the sample for five more days at room temperature enabled the evaporation of solvent and the release of alkoxy groups resulting in a dry product. The obtained sample was subsequently grinded to fine powder and stored. The measurements were taken approximately 1 month after the synthesis.

The powder X-ray diffraction (XRD) was accomplished using Shimadzu diffractometer XRD 6000 with CuKα radiation. Data were collected between 2 and 80° 2θ in a step scan mode with steps of 0.02° and counting time of 0.6 s. Silicon (Aldrich 99.999 %) in amount of 10 mass% was added as internal standard to the samples annealed at various temperatures. The crystallinity of samples was characterized comparing anatase (100) and silicon (111) diffraction peak intensities. The average crystallite size of anatase was calculated from the broadening of (100) diffraction peak using Scherrer's equation: $D = k\lambda/(B\cos\theta)$, where D is the average crystallite diameter, k is Scherrer constant (0.9), λ is the X-ray wavelength (0.15418 nm), B is full width at the half height of (100) diffraction peak corrected for instrumental broadening, and θ is the diffraction angle.

The morphology of the samples was examined using field emission scanning electron microscope (FESEM) JEOL 6500F and high-resolution transmission electron microscope (HRTEM) JEOL JEM-2100.

IR spectra were acquired using the Fourier transform infrared spectrometer Bruker Vertex 70 in ATR (attenuated total reflectance) mode. The samples were pressed on a diamond, and the absorbance data were collected between 400 and 4000 cm^{-1} with spectral resolution of 1 cm^{-1} and 64 scans.

The thermal evolution of gel was characterized with DTA-TG thermal analysis (Netzsch STA 409C thermoanalyzer). For the thermal analysis, ∼ 50 mg of material was placed in Pt crucible and heated at a rate of 10 °C min^{-1} in a synthetic air flow of 30 cm^3 min^{-1}. α-Alumina was used as a reference. FTIR and XRD were used to characterize gel, intermediates and final products of its thermal decomposition.

Surface area of powders was determined by Brunauer–Emmett–Teller (BET) [13] N$_2$ gas adsorption–desorption isotherm obtained at 77 K on the Micromeritics ASAP-2000 equipment. Samples were previously degassed at 100 °C under a dynamic vacuum of 1.3 × 10^{-2} Pa. Pore size distribution was calculated from the desorption isotherm obtained by the BJH model [14].

Results and discussion

The powder X-ray diffraction pattern of the dried gel (Fig. 1) shows low-intensity, very broad line centered at about 23° 2θ, indicating the prepared gel is amorphous. Sample also shows a signal centered at 5.6° 2θ. There are a plethora of semantic variations used in attempts to describe the reason for the occurrence of low-angle peaks in diffraction patterns of titania precursor materials. The appearance of single line at high d-spacing in XRD pattern with no significant wide-angle peaks was interpreted to be due to the formation of material with the degree of order in
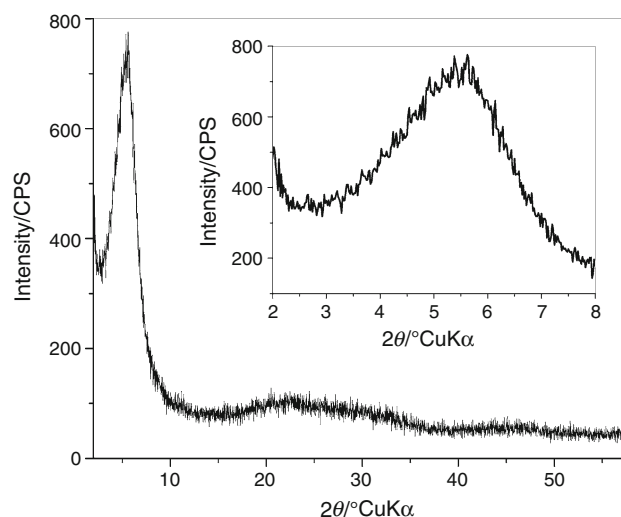

Fig. 1 Powder XRD pattern of dried gel. *Inset* enlarged portion of XRD pattern in 2°–8° 2θ (CuKα) range

the mesostructure [15], material with no long-range mesoscopic ordering [16], disordered mesostructured material [17], non-ordered mesoporous material [18], open-framework disordered material [19], "wormhole"-type material [20] and material with wormhole-like framework mesostructure [21]. Therefore, according to the observed XRD pattern investigated gel could be characterized as mesostructured and the absence of diffraction peaks at higher angles points out to a lack of higher degree of structural order. The sharpness of the low-angle peak would suggest high degree of order in the mesostructure [15, 18]. On the other hand, relatively weak and broad peak, as observed in XRD data, indicates the short range ordering at the mesoscale [15, 18]. It is not clear to what extent classical crystallographic approach is applicable to this type of material [20], but, according to the Bragg equation, the *d*-spacing of repeating units of obtained mesostructured material can be estimated to be 15.8 Å.

To shed more light on the local order of gel samples, field emission scanning electron microscopy and transmission electron microscopy measurements were taken (Fig. 2). FESEM image of the dried gel (Fig. 2a) shows the gel consists of agglomerated particles exhibiting no regularity in morphologies nor dimensions. HRTEM image (Fig. 2b) gains insight in gels mesostructural features where a pattern of dark high electron density spots surrounded by light areas having lower electron density could be seen randomly throughout the specimen. Similar TEM images for sol–gel-derived mesostructured titania, associated with the presence of molecular template, were reported previously in the literature [16, 17, 20, 21]. Light areas could be attributed to the organic moieties present in the gel. Therefore, it appears the gel consists of hybrid inorganic–organic nanoclusters. The nanoclusters are ordered sufficiently enough to yield described single-peak diffraction pattern. As stated earlier from XRD pattern, the *d*-spacing of repeating units of mesostructured material

should be ~ 1.6 nm. Although images were thoroughly examined, no direct relation between XRD low-angle peak and HRTEM distances was observed. However, according to the literature, highly probable outcome of applied synthesis procedure is polynuclear titanium-oxo-alkoxy clusters bearing complexing ligands, $[Ti_xO_y(OR)_z(L)_w]$ [22, 23]. Literature reports numerous and diverse metal-oxo clusters with sizes ranging from 0.5 to 2.5 nm [22]. Specifically, titanium-oxo-alkoxy clusters with Keggin-type structure and similar dimensions were described in the literature [24].

Additional information on gel structure was obtained through FTIR analysis (Fig. 3) of dried gel. The most prominent vibrations in spectrum are those of Eaa. As mentioned before, Eaa has two forms, ketonic and enolic (Fig. 4a). Typical peaks for ketonic form are those at 1710 and 1730 cm^{-1}, assigned to the bending vibration of C=O group. The hydroxylic proton of enol tautomer is easily ionized (Fig. 4a), and typical C=O vibration of enolate, stabilized by chelation with alkoxide (Fig. 4b), occurs at
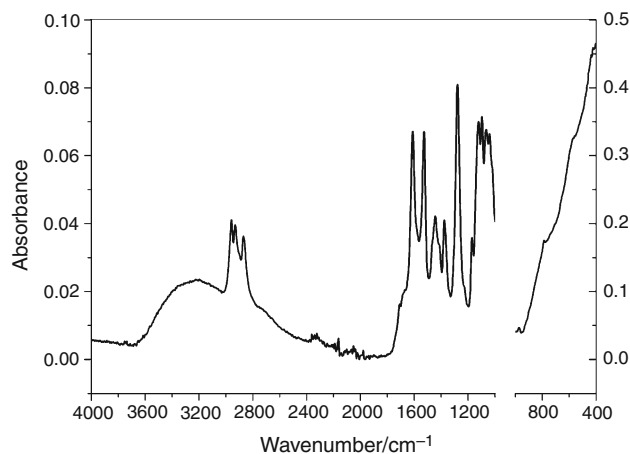

Fig. 3 FTIR spectrum of dried gel

Fig. 2 **a** Field emission electron microscopy image of the dried gel. **b** High-resolution transmission electron microscopy image of the dried gel. *Inset* enlarged portion of dried gel HRTEM image
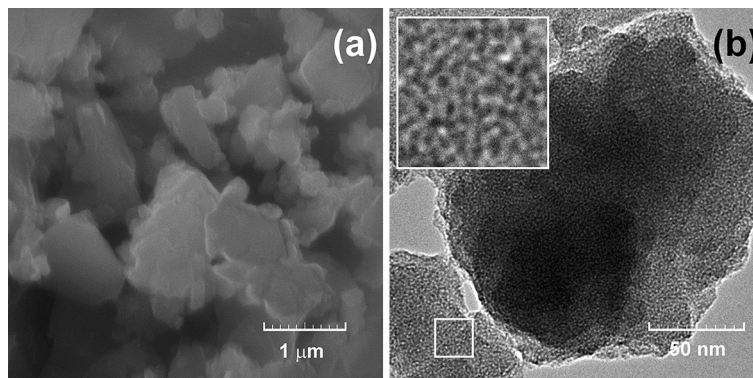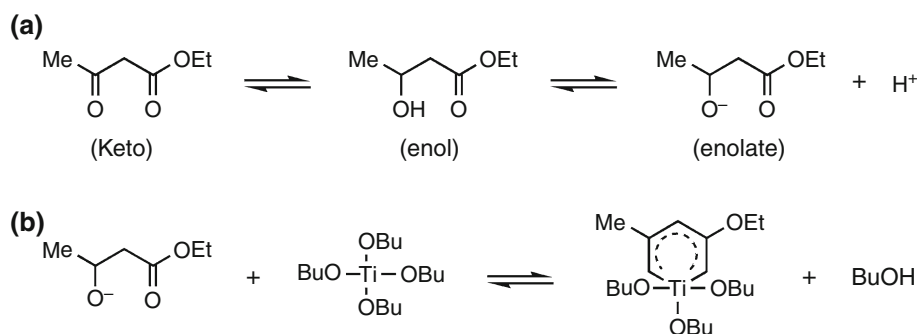
Fig. 4 **a** Keto–enol
tautomerism of ethyl
acetoacetate and formation of
enolate anion, **b** chelation,
formation of the six-membered
chelate ring

1610 to 1530 cm^{-1} [25–27]. As can be seen, both sets of
peaks, very strong vibrations of enolic Eaa chelated to
metal alkoxide and weak bands of ketonic Eaa, can be
observed in spectra of as-received sample. Additionally, a
strong band at 1280 cm^{-1} attributed to stretching in com-
plex ring (Fig. 4b) could be observed. As established ear-
lier [12], in the course of sol–gel synthesis, Eaa was
completely chelated to Tnb and no excess keto tautomer
was present in samples. Therefore, the observation of bands
due to ketonic Eaa is the consequence of partial hydrolysis,
causing the release of Eaa from complex [27].

The spectrum of dried gel also shows a set of three
vibrations at 2960, 2930 and 2870 cm^{-1} corresponding to
symmetric and antisymmetric stretching vibration modes of
–CH$_2$– and –CH$_3$ groups [28–30] and bands at 1440 and
1380 cm^{-1} related to –CH$_3$– and –CH$_2$– deformation
vibrations [28–30].

The Ti–O–C stretching can be observed at 1125 cm^{-1}
[28, 30]. According to Velasco et al. [30] and Bahloul et al.
[28], the absorption bands at 1095 and 1040 cm^{-1} could be
attributed to the –C–O– vibration of alkoxide groups linked
to Ti, while vibration at 1070 cm^{-1} is typical for the titanium
n-butoxide. The bands at 935 and 625 cm^{-1} could be ascri-
bed to vibrational modes of butoxide –CH$_3$– and –CH$_2$–
groups [31]. Those vibrations point out to a presence of
alkoxide predominantly bonded to titanium, but some of
them could also originate from n-butanol released during
hydrolysis [30], although it could be assumed that the
majority of n-butanol released during chelation has been
evaporated from sample.

Finally, the bandwidth between 3700 and 2500 cm^{-1}
centered at ∼3100 cm^{-1} is due to the stretching vibration
of the hydroxyl groups. According to Velasco [30], the
broad band between 3600 and 3000 cm^{-1} is the conse-
quence of several convoluted peaks corresponding to free
or interstitial water, coordinatively bound water and rigidly
bound water in the form of hydroxyl ions (Ti–OH groups),
as well as the presence of OH groups from butanol. The
band due to O–H vibrations of Ti–OH groups is located at
3545 cm^{-1}. The formation of Ti–OH species in the course
of gelation was described in numerous investigations of

similar systems [25, 26, 29, 32]. On the other hand, bands
due to retained H$_2$O and butanol produced by the Tnb
hydrolysis are at 3266 cm^{-1}. The presence of adsorbed
water is also indicated by the occurrence of OH bending
vibration of H$_2$O at 1625 cm^{-1} [25, 28–30].

Therefore, the dried gel can be described as Ti chelate
comprised of unhydrolyzed ethyl acetoacetate and, to a
certain extent, unhydrolyzed butoxy groups, both bonded to
titanium. Further, hydroxy groups bonded to titanium, as a
consequence of replacement of butoxy groups with OH
groups in the course of hydrolysis, are present. Finally, the
formula of hydrolyzed product may include the oxo-
bridges formed through condensation reaction between
butoxy and hydroxy groups [10]. Abovementioned may
turn to be the critical factor for obtaining structural order
on mesoscale. Additionally, along with the obtained hybrid
product, small amounts of n-butanol and keto tautomer of
ethyl acetoacetate, released in the course of hydrolysis, as
well as adsorbed water, are also present in the gel.

Based on the findings from the XRD, TEM and FTIR
analysis, the gels mesostructure can be described as con-
sisted of inorganic–organic nanoclusters that act as
repeating units in the prepared mesostructured gel. The
formation of various chelated species [12] with different
affinity to hydrolysis probably caused polydispersity and
compositional variations of nanoclusters. Random packing
of nanoclusters enabled formation of three-dimensional
mesostructure without long-range ordering, giving rise to a
single broad peak in the low-angle region. Eaa, as most
abundant cluster organic group, plays multiple roles in
acting as the chemical modifier of Tnb lowering its reac-
tivity, as well as influencing the nanocluster structure and
therefore having a key role in the course of mesostructure
development.

In order to confirm those findings and shed more light on
gel structural evolution, a differential thermal and ther-
mogravimetric analysis of dried gel was made. Figure 5
shows the thermal behavior of dried gel by depicting the
DTA, TG and DTG curves. Seven processes were detected
up to 1000 °C: An endothermic processes accompanied
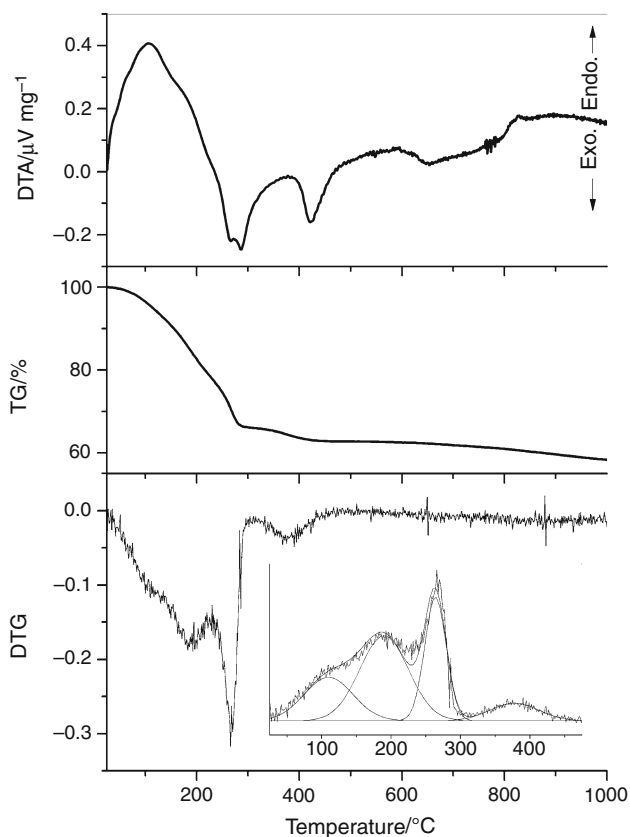with mass losses centered at ∼108 and ∼192 °C, a two-

Fig. 5 DTA, TG, and DTG curves of dried gel obtained with heating rate of 10 °C min^{-1} in air. *Inset* enlarged portion of DTG curve in temperature interval between 25 and 475 °C. *Curve* is fitted to multiple Lorentz peaks
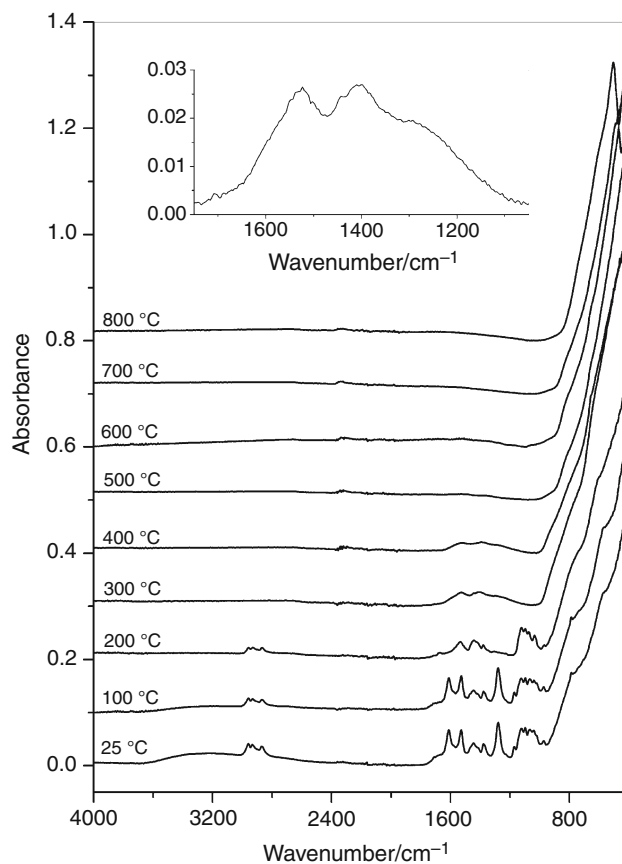

Fig. 6 FTIR spectra of gel samples quenched from various temperatures. Spectra are shifted vertically for visualization purposes. *Inset* enlarged portion of FTIR scan of sample quenched from 300 °C in wave number interval between 1750 and 1050 cm^{-1}

step exothermic process at $\sim$267 and $\sim$287 °C also accompanied with the mass loss, a mass loss at $\sim$380 °C, exothermal peak centered at $\sim$422 °C, a wide exothermal peak between 655 and 800 °C and finally a continuous mass loss in the interval of 600–1000 °C. According to the TG curve, the total mass loss in the temperature interval 25–1000 °C is 41.7 %. The DTG curve is fitted to multiple Lorentz peaks; according to profile fit, mass losses yield 8.1 and 15.8 % for first and second endothermic processes, respectively. Exothermic processes between 200 and 300 °C are accompanied with mass loss of 10.1 %. Mass loss at $\sim$380 °C and continuous mass loss in the interval of 600–1000 °C yield 3.2 and 4.4 %, respectively.

In order to characterize the gel, intermediates and final thermal decomposition products and to assign the observed processes, FTIR and XRD analyses were employed. Samples were quenched from various temperatures in a range of 100–800 °C and analyzed.

FTIR spectra of the samples quenched from various temperatures are presented in Fig. 6. Compared with the as-prepared sample, spectrum of sample quenched from 100 °C shows reduced intensities of vibrations due to a

–CH$_3$– and –CH$_2$– groups. The intensity of broad band between 3600 and 3000 cm^{-1}, corresponding to free or interstitial water, also decreased. However, main absorption peaks exhibit no changes in position or intensity. Therefore, first process resembling endothermic peak with corresponding mass loss occurs as the consequence of adsorbed butanol and water release.

Thermal treatment at 200 °C yields further decrease in bands due to a –CH$_3$– and –CH$_2$– groups as well as H$_2$O bands. More important, thermal treatment at 200 °C brings about the disappearance of chelate ring vibrations, pointing out to the decomposition of chelate as second endothermic process. Instead, bands at 1526 and 1403 cm^{-1} attributed to C=O bond in CO$_2$ adsorption species [33, 34] appear (inset in Fig. 6). Among at least three possible CO$_2$ adsorption species: unidentate carbonate, bidentate carbonate and bicarbonate, bands at 1526 and 1403 cm^{-1} resemble the most to those due to a unidentate carbonate, a symmetric O–C–O stretching at 1360–1400 cm^{-1} and an asymmetric O–C–O stretching at 1510–1560 cm^{-1} [35]. On the other hand, absorption bands in range between 1000 and

1200 cm^{-1} suggest butoxide groups are still bonded to titanium [8]. Therefore, the chelate decomposition can be considered as the most significant feature of second process.

Thermal treatment of the sample from 300 °C yields the disappearance of butoxide bands. The appearance of two overlapped exothermal peaks probably indicates a two-step process. So, third process can be considered as a two-step release and burning of butoxide groups.

The treatment of the sample at 400 °C results in reduction of carbonate vibrations intensity, while treatment at 500 °C brings about complete disappearance of carbonate vibrations. Therefore, fourth process, mass loss centered at ~380 °C is probably due to carbonate desorption. This is in concordance with the findings of Ferreti et al. [35] who observed unidentate carbonates are difficult to remove by thermal treatment.

Sample quenched from 500 °C shows no vibration modes except broad envelope between 400 and 800 cm^{-1}, generally considered to occur due to the presence of Ti–O–Ti network [25, 30, 36], evidencing the condensation reactions and thereafter the formation of the inorganic network [28].

FTIR spectra offer no clue on the nature of processes 5–7. It could be supposed that exothermal peak centered at ~422 °C is due to anatase crystallization, while wide peak between 655 and 800 °C is due to anatase to rutile transformation [37]. Finally, continuous mass loss in the interval of 600–1000 °C seems to correspond to combustion of carbonaceous species formed as a consequence of incomplete oxidation of organics. In order to confirm these assumptions, XRD patterns of samples quenched from various temperatures were acquired.

The structural changes accompanying thermal treatment of gel, over the temperature range 25–800 °C, are summarized in Fig. 7 within the presented X-ray diffractograms.

Heating of samples to 100 °C does not change the appearance of low-angle XRD peak. Peak shows reduced intensity upon heating to 200 °C and vanishes after heating to 300 °C. Sample was still amorphous after heating to 300 °C. Faint and broad peaks indicating low crystallinity could be observed for the sample heated to 400 °C, while thermal treatment to 500 °C leads to the appearance of well-defined diffraction peaks (Fig. 7). All diffraction lines correspond well to those of anatase (ICDD-PDF No. 21-1272). Small improvement of crystallinity, indicating grain growth, was observed after heating to 600 °C. However, at this temperature, a partial phase transformation from anatase to rutile (ICDD-PDF No. 21-1276) was observed. The increase in thermal treatment temperature to 700 °C increased the amount of rutile since higher temperature conditions enabled the phase transformation from thermodynamically metastable anatase to the most stable rutile phase. Finally, sample quenched from 800 °C consists only of rutile so the
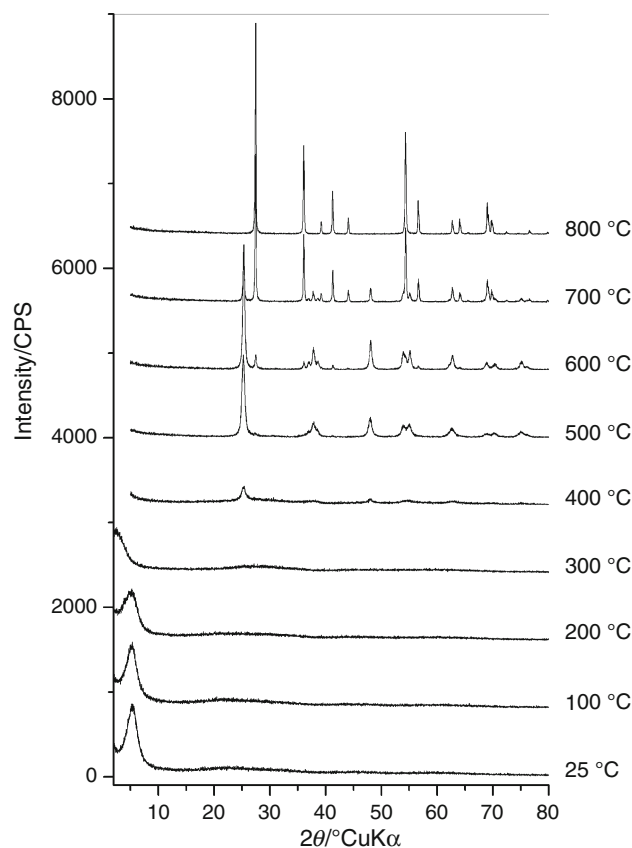

Fig. 7 Powder XRD patterns of gel samples quenched from various temperatures. Spectra are shifted vertically for visualization purposes

processes 5 and 6 could be safely attributed to anatase crystallization and transformation to rutile.

Therefore, on basis of FTIR and XRD analyses, endothermic and exothermal peaks as well as mass losses on DTA/TG scans of gel sample are attributed as follows (Fig. 8): An endothermic process accompanied with the mass loss centered at ~108 °C is caused by elimination of adsorbed water, butanol and ethyl acetoacetate on the grain surface and inside composite particles [6]. A rapid mass loss centered at ~192 °C and also caused by endothermic process was attributed to decomposition of chelate and evaporation of Eaa. Decomposition of butoxide and elimination of butoxy groups occur in all samples between 200 and 300 °C in a two-step process. The collapse of the mesostructure in sample quenched from 300 °C is the obvious consequence of organics removal. In this manner, a key role of butoxide and enolate groups in establishment and maintenance of mesostructure was confirmed.

Mass loss centered at ~380 °C was attributed to carbonate removal. The mass loss in this temperature interval is occasionally attributed to the dehydroxylation of Ti–OH groups formed in the course of hydrolysis [26, 38], but in present investigation, no indication for OH groups presence was found within this temperature interval. The exothermal
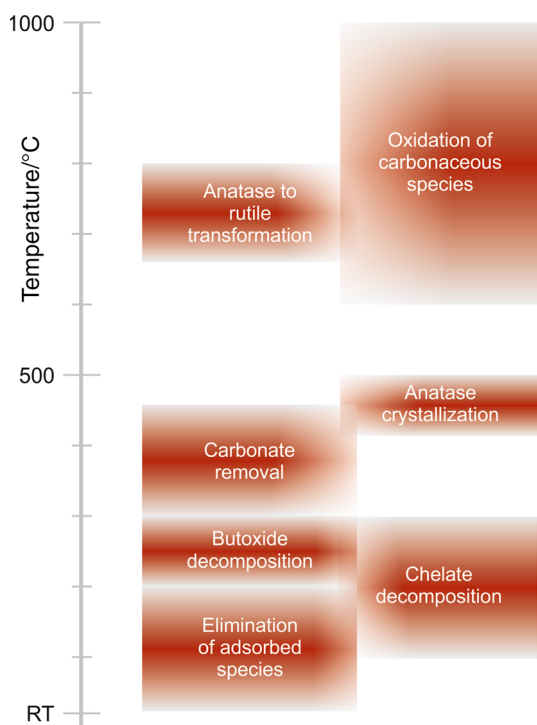
Fig. 8 Scheme of dried gel thermal decomposition process

process, centered at ~422 °C, can safely be attributed to anatase crystallization, whereas following exothermal peak is a consequence of anatase to rutile transformation [36]. Finally, mass loss above 600 °C could be attributed to the oxidation of carbonaceous species remains, i.e., char and tar within powder grains. According to findings of Madarasz et al. [39] in similar system, a slow permanent oxidation of tarred components, accompanied by the release of carbon dioxide, starts above 500 °C and can proceed up to high temperatures. The final gel sample decomposition product above 800 °C is pure rutile.

According to TG sample mass loss is 41.7 %. Although with DTG curve deconvoluted and mass losses of each step determined, it was impossible to even roughly estimate initial composition of gel sample. Few reasons for that are: incomplete decomposition/oxidation process left some carbonate in sample, lack of data on titania-bonded OH groups or oxo-bridges and lack of data on adsorbed species. Yet comparison of achieved mass loss of 41.7 to mass loss of 82 % the sample with nominal composition $Ti(O^{n-}Bu)_2(Eaa)_2$ would exhibit, brings about the conclusion the sample hydrolysis was moderate.

As shown in Fig. 7, a partial crystallization of anatase occurred after quenching from 400 °C to be completed after quenching from 500 °C. However, higher temperatures increase the tendency of crystal growth and can lead to nanocrystals sintering. On the other hand, prolonged thermal treatment is expected to improve crystallization

without the need of temperature increase. Hence, to achieve complete crystallization at lower temperatures without exaggerated crystal growth and sintering, gel was thermally treated at various temperatures between 300 and 450 °C for 2 h.

XRD patterns of samples thermally treated at temperatures between 300 and 450 °C for 2 h are shown in Fig. 9. As can be seen, the traces of anatase appear even after thermal treatment at temperature as low as 300 °C. Treatment at 350 °C leads to the appearance of well-defined but broad diffraction peaks pointing out to nanocrystalline character of pure anatase. Other polymorphs of titania (i.e., peaks at 2θ angles of 27.5° due to the (110) reflection of rutile and 30.8° due to the (121) reflections of brookite, respectively) were not observed. Titania phases; anatase; and rutile are commonly used in photocatalysis, whereas anatase phase shows higher photocatalytic activity [29], so obtaining pure anatase is desirable. The sample thermally treated at 400 °C still consists of pure anatase, yet diffraction peaks narrowed slightly. Rutile traces could be observed in sample thermally treated at 450 °C (Fig. 9). It should be noted that even the thermal treatment at 450 °C for 2 h was not sufficient for complete organics phase removal, as evidenced from grayish color of samples. Grayish color of samples was ascribed to carbonaceous deposits derived from the decomposition of organic and encapsulated by the titania matrix, making its decomposition difficult [18]. This observation is in concordance with TG results showing the presence of organic residue thermal decomposition products at high temperatures [40].

As thermal treatment temperature increased, the peaks of anatase phase became stronger and sharper, indicating better crystallinity. To quantify the anatase crystal size, anatase (101) diffraction peaks were analyzed by employing the Scherrer equation. The results of crystallite size analysis are presented in Table 1. As can be seen, the average crystal sizes of anatase decrease with annealing temperature increase. Also, anatase crystals in samples thermally treated at various temperatures were quantitatively compared by comparison of areas under (101) anatase peak and (111) silicon peak. The results of semiquantitative analysis are also presented in Table 1. As can be seen, thermal treatment at temperatures higher than 350 °C yields no additional anatase crystallization. In sample thermally treated at 450 °C, peak area, i.e., the quantity of anatase, reduced due to commencement of anatase to rutile transformation.

Figure 10a shows FESEM micrograph of sample thermally treated at 350 °C for 2 h, revealing it consists of aggregated irregular grains. A HRTEM image (Fig. 10b) confirms the mesostructure of the material collapsed after organic removal by calcinations, as expected on the basis of XRD data. In HRTEM image, grains consisting of nanocrystals and possibly some amorphous phase could be

Fig. 9 Powder XRD pattern of sample thermally treated at various temperatures for 2 h. *Inset* enlarged portion of XRD pattern of sample quenched from 450 °C in 2θ interval between 23.5 and 30° CuKα. *A* Anatase, *R* rutile, *S* silicon
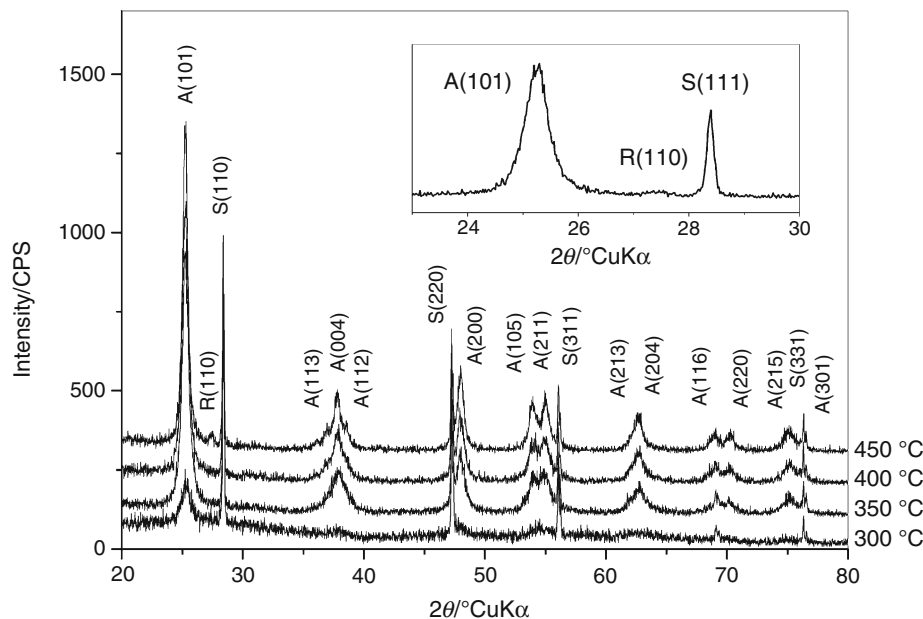

Table 1 Crystallite size, intensity quotient of (101) peak of anatase and (111) peak of silicon, specific surface area and pore volume of samples thermally treated at various temperatures for 2 h

Thermal treatment temperature/°C	Crystallite size/nm	$I_A(101)/I_S(111)$	Specific surface area/m^2 g^{-1}	Pore volume/cm^3 g^{-1}
300	18	1.64	14.21	0.0189
350	16	7.94	26.09	0.0332
400	16	7.92	15.63	0.0273
450	16	7.61	–	–

observed. Furthermore, lattice fringes with the *d*-spacing of ∼0.35 nm can clearly be observed throughout the HRTEM image (inset in Fig. 10b). The 0.35-nm interval corresponds to interplanar spacing of anatase crystal structure (101) plane, i.e., to {101} facets. Common anatase crystal represents slightly truncated tetragonal bipyramid where majority of exposed surface resemble {101} facets. The exposed {101} anatase facet is thermodynamically most stable, i.e., resemble surface with the lowest average energy [41]. Although the majority of fringes throughout the area observed corresponds to (101) plane, fringes with spacing of ∼0.24 nm (Fig. 10b inset), corresponding to (004) plane, were also observed.

BET adsorption of nitrogen gas for surface area determination at the temperature of liquid nitrogen was performed on samples thermally treated at 300, 350 and 400 °C for 2 h. Adsorption–desorption isotherms are presented in Fig. 11, while surface area and pore volume are listed in Table 1. Nitrogen adsorption–desorption isotherms of sample thermally treated at 300 °C (Fig. 11) exhibit a type II isotherm (IUPAC, 1985) which is most frequently encountered for adsorption on non-porous powders. This sample is

characterized with low specific surface area of 14.21 m^2 g^{-1}, which is consequence of low pore volume of 0.0189 cm^3 g^{-1} (Table 1). As can be seen in Fig. 11, pore size distribution has no maximum pointing out to a texture that resembles gel prior to thermal treatment.

On the other hand, samples thermally treated at 350 and 400 °C for 2 h exhibit a type IV isotherm with a H2 hysteresis loops indicating the presence of mesopores [42, 43]. This type of hysteresis loop is believed to be associated with pores generated by agglomerates or compacts of particles of non-uniform size and arrangement [44]. This is the precise description of the microstructure displayed in FESEM micrograph in Fig. 10a, so it can be safely said that texture is decisively determined by particle agglomeration.

Sample treated at 350 °C possesses the highest specific surface area, 26.09 m^2 g^{-1}. Appreciable decrease in specific surface area to 15.63 m^2 g^{-1} (Table 1) was observed with the increase in thermal treatment temperature. Those values are in concordance with the values of pore size volume being 0.0332 and 0.0273 cm^3 g^{-1} for samples thermally treated at 350 and 400 °C, respectively.

Fig. 10 a Field emission scanning electron microscopy image of sample thermally treated at 350 °C for 2 h. b High-resolution transmission electron microscopy image of sample thermally treated at 350 °C for 2 h. *Insets* enlarged portions of thermally treated sample HRTEM image showing *d*-spacings of 0.351 and 0.235 nm
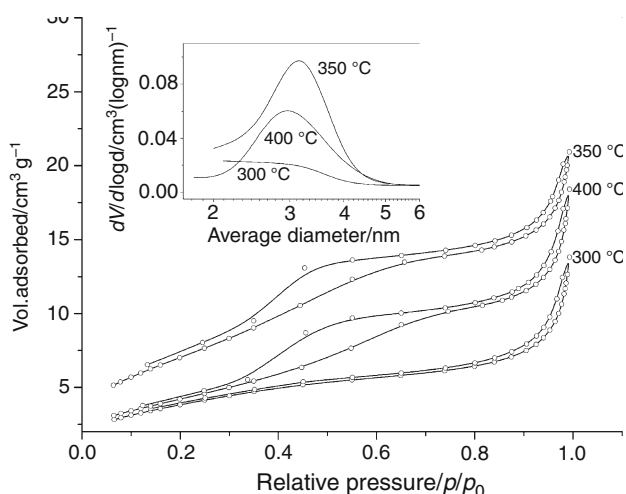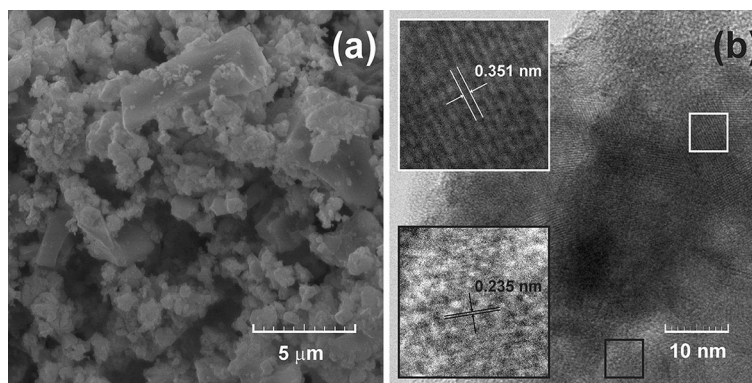

Fig. 11 N₂ adsorption–desorption isotherms of samples thermally treated at 300, 350 and 400 °C for 2 h. *Inset* presize distribution calculated from desorption isotherm by the BJH model

Low surface area of both samples suggests poor pore structure. The BJH analysis for the samples yields corresponding pore size distribution peaks in the range from 2 to 5 nm (Fig. 11). The pore volume increase in sample thermally treated at 350 °C in comparison with sample thermally treated at 300 °C could be attributed to the removal of the residual organic phase in pores. The same phenomenon brings about the increase in specific surface area. On the other hand, the decrease in specific surface area and pore volume, with the increase in thermal treatment temperature to 400 °C, is due to improved sintering, which is a quite common observation. Generally, low surface area of samples is the consequence of low pore volume which could be attributed to partial blocking of the pores with residual carbonaceous material. The residuals of carbonaceous material were observed using TG analysis, and the

reduction in pore volume due to blockage with carbonaceous material was described in the literature [45].

Conclusions

Titania gel was prepared by chelation of titanium *n*-butoxide with ethyl acetacetate in 1:1 ratio followed with slow hydrolysis. FTIR spectrum and TG scan of gel pointed out to partial hydrolysis of chelate, leaving some residual butoxy and ethyl acetoacetate groups attached to titanium. XRD patterns and HRTEM micrographs of the gel revealed some degree of ordering at mesostructure scale. The gels mesostructure consisted of inorganic–organic nanoclusters, exhibiting some polydispersity in the size and variations in composition. The random packing of nanoclusters enables development of three-dimensional mesostructured framework, giving rise to a single broad peak in the low-angle region.

Thermal decomposition of the complex in air up to 1000 °C shows seven decomposition steps: evaporation of water and butanol at ∼108 °C, elimination of ethyl acetoacetate at ∼192 °C and butoxy groups between 200 and 300 °C, carbonate removal at 380 °C, crystallization of anatase at 422 °C, its transformation to rutile between 655 and 800 °C and, finally, oxidation of carbonaceous species between 600 and 1000 °C. Thermal treatment at 200 °C yields collapse of the mesostructure and disappearance of low-angle XRD peak.

In samples thermally treated at 300 °C for 2 h, the formation of nanocrystalline anatase was observed. The improvement of crystallinity was observed after thermal treatment at 350 °C, while a minute partial phase transformation from anatase to rutile was observed for sample thermally treated at 450 °C. The average crystallite size of sample thermally treated at 350 °C was found to be 16.4 nm.

Nitrogen absorption–desorption isotherms and pore size distribution of sample thermally treated at 350 °C for 2 h are typical of porous aggregates of anatase nanocrystals, with a relatively narrow pore size distribution in the range of mesopores. Relatively low specific surface area of sample, $26.09 \text{ m}^2 \text{ g}^{-1}$, was ascribed to reduction in mesopores volume due to blockage with carbonaceous material which cannot be removed by thermal treatment at temperature as low as 350 °C for 2 h.

A nanocrystalline character of prepared anatase was confirmed through HRTEM micrographs.

References

1. Chen X, Mao SS. Titanium dioxide nanomaterials: synthesis, properties, modifications, and applications. Chem Rev. 2007;107:2891–959.
2. Liu Y, Liu CY, Zhang ZY. Effects of carboxylic acids on the microstructure and performance of titania nanocrystals. Chem Eng J. 2008;138:596–601.
3. Porkodi K, Arokiamary SD. Synthesis and spectroscopic characterization of nanostructured anatase titania: a photocatalyst. Mater Charact. 2007;58:495–503.
4. Lu C-W, Cao Y, Li H, Webb C, Pan W-P. Synthesis of TiO$_2$ based on hydrothermal methods using elevated pressures and microwave conditions. J Therm Anal Calorim. 2014;116:1241–8.
5. Nolan NT. Sol–gel synthesis and characterisation of novel metal oxide nanomaterials for photocatalytic applications. PhD Dissertation. Dublin Institute of Technology; 2010.
6. You JH, Hsu KY. Influence of chelating agent and reaction time on the swelling process for preparation of porous TiO$_2$ particles. J Eur Ceram Soc. 2010;30:1307–15.
7. Birnie DP III, Bendzko NJ. ^{1}H and ^{13}C NMR observation of the reaction of acetic acid with titanium isopropoxide. Mater Chem Phys. 1999;59:26–35.
8. Errington RJ, Ridland J, Clegg W, Coxall RA, Sherwood JM. β-diketonate derivatives of titanium alkoxides: X-ray crystal structures and solution dynamics of the binuclear complexes [{Ti(OR)$_3$(dik)}$_2$]. Polyhedron. 1998;17:659–74.
9. Jung MW, Oh HJ, Yang JC, Shul YG. Structural investigation of the hydrolysis-condensation process of modified titanium isopropoxide. Bull Korean Chem Soc. 1999;20:1394–8.
10. Kayan A, Hoebbel D, Schmidt H. Complexation of titanium alkoxides with pentenoic acid and allylacetoacetate and their hydrolysis and addition reactions with H-silanes. J Appl Poly Sci. 2005;95:790–6.
11. Kurajica S, Mali G, Gazivoda T, Sipusic J, Mandic V. A spectroscopic study of calcium aluminate gels obtained from aluminium sec-butoxide chelated with ethyl acetoacetate in various ratios. J Sol-Gel Sci Technol. 2009;50:58–68.
12. Kurajica S, Škorić I, Lozić I, Mandić V. Ethyl acetoacetate ligand distribution in the course of titanium *n*-butoxide chelation. Mater Chem Phys. 2014;147:1058–67.
13. Brunauer S, Emmett PH, Teller E. Adsorption of gasses in multimolecular layers. J Am Chem Soc. 1938;60:309–19.
14. Barrett EP, Joyner LG, Halenda PP. The determination of pore volume and area distributions in porous substances. I. Computations form nitrogen isotherms. J Am Chem Soc. 1951;73:373–80.
15. Chen W, Qiu Y, Yan K, Yang S. Surfactant directed self-assembly of size-tunable mesoporous titanium dioxide microspheres and their application in quasi-solid state dye-sensitized solar cells. J Power Sources. 2011;196:10806–16.
16. Chandra D, Bhaumik A. Photoluminescence behavior of new mesoporous titanium-composites synthesized by using bidentate structure directing agents. Micropor Mesopor Mater. 2007;101:348–54.
17. Chandra D, Bhaumik A. Super-macroporous TiO$_2$ synthesized by using new designed chelating structure directing agents. Micropor Mesopor Mater. 2008;112:533–41.
18. Saadoun L, Ayllon JA, Jimenez-Becerril J, Peral J, Domenech X, Rodriguez-Clemente R. Synthesis and photocatalytic activity of mesoporous anatase prepared from tetrabutylammonium–titania composites. Mater Res Bull. 2000;35:193–202.
19. Sarkar K, Laha SC, Mala NK, Bhaumik A. A porous open-framework titanium oxophenylphosphate. J Solid State Chem. 2008;181:2065–72.
20. Dag O, Soten I, Celik O, Polarz S, Coombs N, Ozin GA. Solventless acid-free synthesis of mesostructured titania: nanovessels for metal complexes and metal nanoclusters. Adv Funct Mater. 2003;13:30–6.
21. Wang YD, Ma CL, Sun XD, Li HD. Synthesis and characterization of amorphous TiO$_2$ with wormhole-like framework mesostructured. J Non-Cryst Solids. 2003;319:109–16.
22. Rozes L, Steunou N, Fornasieri G, Sanchez C. Titanium-oxo clusters, versatile nanobuilding blocks for the design of advanced hybrid materials. Monatsh Chem. 2006;137:501–28.
23. Kim YT, Park YS, Myung H, Chae HK. A chelate-assisted route to anatase TiO$_2$ nanoparticles in acidic aqueous media. Colloids Surf A. 2008;313–314:260–3.
24. Azouani R, Soloviev A, Benmami M, Chhor K, Bocquet JF, Kanaev A. Stability and growth of titanium-oxo-alkoxy Ti$_x$O$_y$(-OiPr)$_z$ clusters. J Phys Chem C. 2007;111:16243–8.
25. Chen HJ, Wang L, Chiu WY. Chelation and solvent effect on the preparation of titania colloids. Mater Chem Phys. 2007;101:12–9.
26. Chang TC, Wang YT, Hong YS, Chiu YS. Effects of inorganic components on the structure and thermo-oxidative degradation of PMMA modified metal alkoxide-EAA complex. Thermochim Acta. 2002;390:93–102.
27. Hoebbel D, Reinert T, Schmidt H. NMR and IR spectroscopic examination of the hydrolytic stability of organic ligands in metal alkoxide complexes and of oxygen bridged heterometal bonds. Mater Res Soc Symp Proc. 1996;435:461–7.
28. Bahloul W, Bounor-Legare V, Seytre G, Cassagnau P. Influence of a non-polar medium (alkane and molten polypropylene) on the titanium *n*-butoxide hydrolysis-condensation reactions. J Sol-Gel Sci Technol. 2011;57:86–94.
29. García-Benjume ML, Espitia-Cabrera MI, Contreras-García ME. The effect of synthesis parameters on the production of titania nanostructured spherical aggregates. J Ceram Proc Res. 2010;11:198–203.
30. Velasco MJ, Rubio F, Rubio J, Oteo JL. DSC and FT-IR analysis of the drying process of titanium alkoxide derived precipitates. Thermochim Acta. 1999;326:91–7.
31. Silverstein RM, Webster FX. Spectrometric identification of organic compounds. 6th ed. New York: Willey; 1998.
32. Jung M. Synthesis and structural analysis of Au-doped TiO$_2$/SiO$_2$ mixed oxide films prepared by sol–gel process. J Sol-Gel Sci Technol. 2000;19:563–8.
33. KrishnaChandar N, Jayavel R. Synthesis and photoluminescence properties of HMT passivated Dy$_2$O$_3$ nanoparticles. Phys E. 2012;44:1315–9.
34. Takanabe K, Aika K, Seshan K, Lefferts L. Sustainable hydrogen from bio-oil—steam reforming of acetic acid as a model oxygenate. J Catal. 2004;227:101–8.

35. Ferretti CA, Soldano A, Apesteguia CR, Di Cosimo JI. Mono-glyceride synthesis by glycerolysis of methyl oleate on solid acid–base catalysts. Chem Eng J. 2010;161:346–54.

36. Krunks M, Oja I, Tõnsuaadu K, Es-Souni M, Gruselle M, Niinistö L. Thermoanalytical study of acetylacetonate-modifyed titanium (IV) isopropoxide as precursor for TiO$_2$ films. J Therm Anal Calorim. 2005;80:483–8.

37. Wang M, Wen Y, Sawada Y, Hoshi Y, Hou Z. Effect of oxygen and WO$_3$ additive on anatase-to-rutile phase transformation in TiO$_2$ nanoparticles. J Therm Anal Calorim. 2015;119:435–9.

38. Cernea M, Valsangiacom C, Trusca R, Vasiliu F. Synthesis of iron-doped anatase TiO$_2$ powders by a particulate sol-gel route. J Optoelectron Adv Mater. 2007;9:2648–52.

39. Madarasz J, Braileanu A, Crisan M, Pokol G. Comprehensive evolved gas analysis (EGA) of amorphous precursors for S-doped titania by in situ TG–FTIR and TG/DTA–MS in air: part 2. Precursor from thiourea and titanium(IV)-*n*-butoxide. J Anal Appl Pyrolysis. 2009;85:549–56.

40. Ying L, Hon LS, White T, Withers R, Hai LB. Controlled nanophase development in photocatalytic titania. Mater Trans. 2003;44:1328–32.

41. Zhao X, Jin W, Cai J, Ye J, Li Z, Ma Y, Xie J, Qi L. Shape- and size-controlled synthesis of uniform anatase TiO$_2$ nanocuboids enclosed by active 100 and 001 facets. Adv Funct Mater. 2011;21:3554–63.

42. Jitputti J, Pavasupree S, Suzuki Y, Yoshikawa S. Synthesis and photocatalytic activity for water-splitting reaction of nanocrystalline mesoporous titania prepared by hydrothermal method. J Solid State Chem. 2007;180:1743–9.

43. Huang D, Luo G, Yang L, Wang Y. Synthesis of mesoporous TiO$_2$ materials with high specific area using inorganic acids as catalysts. Chin Particuol. 2005;3:176–80.

44. Bajunajdad A, Zaki MI, Eastoe J, Pasupulety L. Characterization of *nano*-cerias synthesized in microemulsions by N$_2$ sorptiometry and electron microscopy. J Colloid Interface Sci. 2006;302:501–8.

45. Kartini I, Lu GQ. Study of the formation of mesoporous TiO$_2$ using isopropoxide precursors under less water conditions. Indo J Chem. 2005;5:15–22.